LETTER

doi:10.1038/nature13137

Quantum chaos in ultracold collisions of gas-phase erbium atoms

Albert Frisch[1], Michael Mark[1], Kiyotaka Aikawa[1], Francesca Ferlaino[1], John L. Bohn[2], Constantinos Makrides[3], Alexander Petrov[3,4,5] & Svetlana Kotochigova[3]

Atomic and molecular samples reduced to temperatures below one microkelvin, yet still in the gas phase, afford unprecedented energy resolution in probing and manipulating the interactions between their constituent particles. As a result of this resolution, atoms can be made to scatter resonantly on demand, through the precise control of a magnetic field[1]. For simple atoms, such as alkalis, scattering resonances are extremely well characterized[2]. However, ultracold physics is now poised to enter a new regime, where much more complex species can be cooled and studied, including magnetic lanthanide atoms and even molecules. For molecules, it has been speculated[3,4] that a dense set of resonances in ultracold collision cross-sections will probably exhibit essentially random fluctuations, much as the observed energy spectra of nuclear scattering do[5]. According to the Bohigas–Giannoni–Schmit conjecture, such fluctuations would imply chaotic dynamics of the underlying classical motion driving the collision[6–8]. This would necessitate new ways of looking at the fundamental interactions in ultracold atomic and molecular systems, as well as perhaps new chaos-driven states of ultracold matter. Here we describe the experimental demonstration that random spectra are indeed found at ultralow temperatures. In the experiment, an ultracold gas of erbium atoms is shown to exhibit many Fano–Feshbach resonances, of the order of three per gauss for bosons. Analysis of their statistics verifies that their distribution of nearest-neighbour spacings is what one would expect from random matrix theory[9]. The density and statistics of these resonances are explained by fully quantum mechanical scattering calculations that locate their origin in the anisotropy of the atoms' potential energy surface. Our results therefore reveal chaotic behaviour in the native interaction between ultracold atoms.

In the common perception, atoms are regarded as 'simple' systems in sharp contrast to 'complex' molecules, whose behaviour is dictated by many (rotational and vibrational) degrees of freedom. The recent realization of dipolar Bose–Einstein condensates and Fermi gases of magnetic lanthanides[10–13] made a novel class of atoms available in the ultracold regime. These exotic species, such as erbium (Er), make it possible to bridge the enormous conceptual gap between 'simple' atoms and molecules, potentially providing a natural test-bed with which to explore complex scattering dynamics in a controlled environment. The rich scattering behaviour of lanthanides has been pointed out in pioneering experiments at millikelvin temperatures[14,15] and theoretical work on cold collisions of atoms with non-zero angular momenta[16,17].

The wealth of intriguing properties of Er, which is the focus of this Letter, originates in its exotic electronic configuration. Erbium is a submerged-shell atom with electron vacancies in the inner anisotropic $4f^{12}$ shell, which lies beneath a filled $6s^2$ shell. As a consequence, it not only has a large magnetic moment, of 7 Bohr magnetons (μ_B), but also has large electronic orbital and total angular momentum quantum number, of $L = 5$ and $J = 6$, respectively; we note that for bosonic and fermionic isotopes the nuclear angular quantum numbers are $I = 0$ and $I = 7/2$, respectively. Large values of L and J are sources of anisotropy in the interatomic interaction. Moreover, the two-body scattering is controlled by as many as 91 electronic Born–Oppenheimer (B–O) interaction potentials, each potential accounting for a specific orientation of J with respect to the internuclear axis (Methods). All B–O potentials are anisotropic and include, at large internuclear separations, a strong dipole–dipole interaction and anisotropic van der Waals dispersion potentials. This situation is in contrast to that of conventional ultracold atoms, such as alkali-metal atoms, where the scattering is determined mainly by the isotropic singlet and triplet B–O potentials[2]. Recent theoretical work predicted the existence of anisotropy-induced Fano–Feshbach resonances in magnetic lanthanides[18]. This greater complexity brings significant new challenges in understanding and exploiting scattering processes.

Our experimental study is based on high-resolution trap-loss spectroscopy of Fano–Feshbach resonances in an optically trapped ultracold sample of Er atoms in the energetically lowest magnetic Zeeman sublevel. We prepare the ultracold sample by following a similar cooling and trapping approach to that described in ref. 12 for bosons and ref. 13 for fermions (Methods Summary). After the preparation procedure, the ultracold sample typically contains about 10^5 atoms at a temperature of around 400 nK. High-resolution trap-loss spectroscopy consists of many experimental cycles. In each cycle, we ramp the magnetic field to a target value, B, and hold the atoms for 400 ms in the optical dipole trap, during which time they undergo elastic and inelastic collisions. To probe the loss of atoms from the trap, we record the atom number by applying standard time-of-flight absorption imaging at zero magnetic field. In the next experimental cycle, we vary the magnetic field value from 0 to 70 G in steps of a few milligauss and repeat the measurement. Figure 1 shows the respective loss spectra for ^{168}Er and ^{166}Er. For both isotopes, we observe very many resonant loss features, which we interpret as being caused by Fano–Feshbach resonances[2]. We identify 190 resonances for ^{168}Er and 189 resonances for ^{166}Er, meaning that we observe about 3 resonances per gauss. We performed similar spectroscopic measurements with the fermionic isotope ^{167}Er, revealing a much higher density of resonances that exceeds 20 resonances per gauss (Extended Data Fig. 1). The fermionic case is complicated by its additional hyperfine structure and detailed studies will be subject of future work.

The very high density of resonances in Er is without precedent in ultracold quantum gases. For comparison, the density of resonances observed in experiments with ultracold alkali-metal atoms or even mixtures is about two orders of magnitude lower than that in Er (compare with refs 19, 20). In Er, it is unclear whether a quantitative mapping of the observed resonances is possible at all. In principle there are at least 91 unknown parameters, corresponding to the phase shifts introduced by the B–O potentials[18]. Instead, we focus our theoretical analysis on fundamental issues, such as whether the observed density of resonances can be reproduced by microscopic calculations, and whether

[1]Institut für Experimentalphysik, Universität Innsbruck, 6020 Innsbruck, Austria. [2]JILA, University of Colorado and National Institute of Standards and Technology, Boulder, Colorado 80309-0440, USA. [3]Department of Physics, Temple University, Philadelphia, Pennsylvania 19122, USA. [4]St Petersburg Nuclear Physics Institute, Gatchina 188300, Russia. [5]Division of Quantum Mechanics, St Petersburg State University, St Petersburg 198904, Russia.

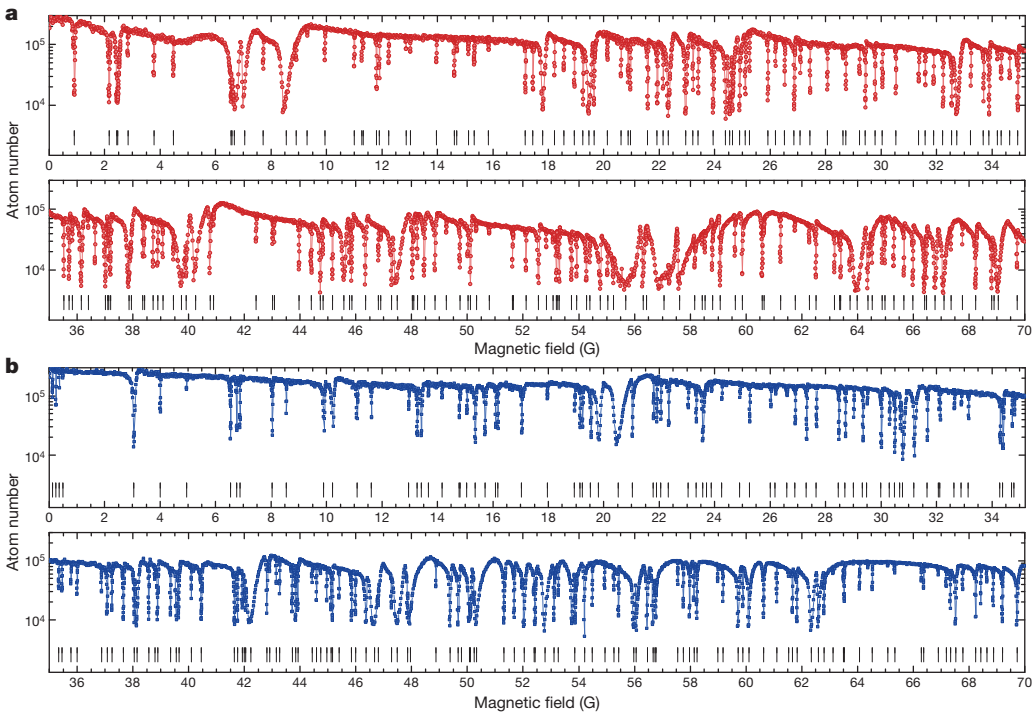

Figure 1 | Fano–Feshbach spectrum of ^{168}Er and ^{166}Er from 0 to 70 G. The trap-loss spectroscopy is performed in an optically trapped sample of Er atoms in the energetically lowest Zeeman sublevel, $m_J = -6$, at a temperature of 330 nK. The atom number is measured after a holding time of 400 ms. We observe 190 Fano–Feshbach resonances for ^{168}Er (**a**) and 189 resonances for ^{166}Er (**b**). Resonance positions are extracted by fitting a Gaussian shape to individual loss features; a full list is given in Extended Data Tables 1 and 2.

our results imply the presence of highly anisotropic interactions, which call into play resonant states of high orbital momentum. We answer these questions in the affirmative using full coupled-channel calculations, supported by an analytical model.

We construct a first-principles coupled-channel model for Er + Er scattering to calculate the spectrum of Fano–Feshbach resonances. Following ref. 18, our model uses the atomic basis set and Hamiltonian (Methods) that includes the radial kinetic and rotational energy operators, the Zeeman interaction and the 91 anisotropic B–O potentials. For small interatomic separations, R, the B–O potentials are calculated using the *ab initio* relativistic, multi-reference configuration–interaction method[21]. At intermediate to large values of R, the B–O potentials are expressed as a sum of multipolar interaction terms. The van der Waals dispersion interaction potentials ($\propto 1/R^6$) are determined from experimental data on atomic transition frequencies and oscillator strengths[22,23]. An important point is that the dispersion potentials have both isotropic and anisotropic contributions. The latter comes from the non-S state character of the Er electronic ground state. The B–O potentials thus induce either isotropic (ℓ and m_ℓ conserving) or anisotropic (ℓ or m_ℓ changing) couplings. Here, ℓ and m_ℓ are the partial-wave quantum number and its projection on the magnetic field quantization axis.

We perform coupled-channel calculations for bosonic ^{168}Er, considering s-wave ($\ell = 0$) collisions and couplings to molecular states with even ℓ up to $L_{\max} = 20$. We calculate the elastic collisional rate coefficient as a function of magnetic field to obtain the Fano–Feshbach resonance spectrum. For $L_{\max} = 20$, we observe a very dense resonance spectrum with about 1.5 resonances per gauss, which qualitatively reproduces our experimental observation (Extended Data Fig. 2). We note that resonances belonging to incident channels with $\ell > 0$ are substantially narrower and do not contribute much to the density of resonances. To get deeper insight into the role of the anisotropy of the potentials, we calculate the mean density of resonances, $\bar{\rho}$, from our coupled-channel calculations for different values of the maximum partial wave $L_{\max}$ (Fig. 2). For $L_{\max}$ up to 20, we observe that $\bar{\rho}$ increases with $L_{\max}$ in a quadratic manner. This dependence stands in stark contrast to alkali-metal atoms, where high-ℓ resonances tend to be too narrow to be observed.

Because our limited computational resources do not allow us to perform calculations for $L_{\max} > 20$, it is worth estimating the density of resonances in a simpler way, based on the separated atom quantum numbers[3]. The key ideas of our model are the following. For each channel $|j_1 m_{J,1}, j_2 m_{J,2}, \ell m_\ell\rangle$, we define the long-range potential $-C_6/R^6 + \hbar^2\ell(\ell+1)/2\mu R^2 + g\mu_B(m_{J,1} + m_{J,2})B$, where C_6 is the isotropic van der Waals coefficient of the B–O potentials and $\hbar$ is Planck's constant divided by 2π. Here μ is the reduced mass, g is the atomic g-factor and, for ground-state Er, $C_6 = 1{,}723$ atomic units (a.u.). Fano–Feshbach resonances in our open channel with $m_{J,1} = -6$ and $m_{J,2} = -6$ are due to couplings to the most weakly bound rovibrational level of closed channels. For a van der Waals potential[2,24] this bound state has a binding energy that must fall within the ℓ-dependent energy window $[-\Delta_\ell, 0]$ with $\Delta_\ell > 0$. The short-range potentials are not accurately known and, for each closed channel, there is a probability dE_b/Δ_ℓ of finding a bound state with a binding energy between E_b and $E_b + dE_b$. From ref. 24 and numerical simulations, we find $\Delta_\ell/E_{vdW} \approx 38.7 + 25.5\ell + 3.17\ell^2$, where $E_{vdW} = \hbar^2/2\mu x_{vdW}^2$ and $x_{vdW} = \sqrt[4]{2\mu C_6/\hbar^2}/2$. Each closed channel contributes $g\mu_B\delta m/\Delta_\ell$ to the mean resonance density, where $g\mu_B\delta m > 0$ is the magnetic-moment difference of the closed and open channels and δm is their difference in molecular projection quantum numbers. Adding the contributions for the closed channels gives the total mean resonance density. This simple counting technique, which we here name random quantum defect theory (RQDT), yields the mean density of resonances shown in Fig. 2. For $L_{\max} \leq 20$, the results of our analytic RQDT agrees very well with the exact coupled-channel calculations. For larger values of $L_{\max}$, the density of resonances keeps growing and eventually saturates to a value around $\rho \approx 4\,G^{-1}$, which is close to the one observed in the experiment. RQDT shows that at least 40 partial waves need to be considered to reproduce the experimental observations.

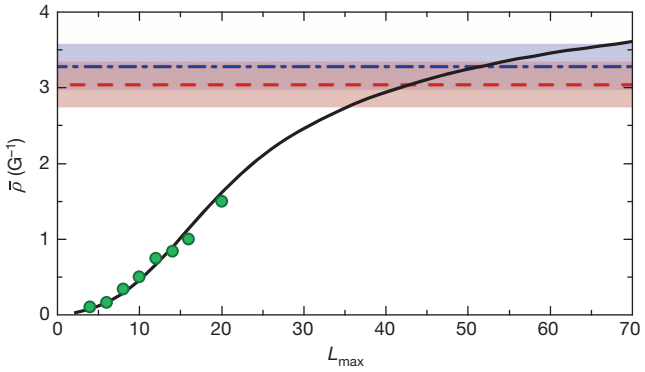

Figure 2 | Mean resonance density for bosonic Er as a function of largest included partial-wave L_{max}. Coupled-channel calculations for L_{max} up to 20 (circles) and RQDT calculation (solid line) for a magnetic field of 0 to 70 G. For calculations, a collision energy of $E = k_B \times (360\ \mathrm{nK})$ is assumed. The mean densities of resonances measured in the experiment are shown for ^{168}Er (dashed line) and for ^{166}Er (dash–dot line) with 1σ confidence bands (shaded areas).

Our microscopic models reproduce well the qualitative behaviour of the system. However, given the complexity of the scattering, the analysis of ultracold collision data can and should no longer aim to assign individual resonances, and the fundamental question of how to tackle complex scattering arises. Historically, spectra of great complexity have been understood within the framework of random matrix theory (RMT), as originally developed by Wigner to describe heavy nuclei containing a very large number of degrees of freedom[25]. This is an alternative view of the quantum mechanics of complex systems, where individual energy levels and resonances are not theoretically reproduced one by one, yet their statistics can be described[26]. RMT characterizes spectra by fluctuations of their energy levels and classifies their statistical behaviour in terms of symmetry classes; for example, the Gaussian-orthogonal ensemble (GOE) is appropriate in the case of a system with time-reversal symmetry, such as neutral atoms.

Following RMT, the distribution of spacings between neighbouring levels (or resonances) characterizes the spectral fluctuations of the system and reflects the absence or the presence of level correlations in terms of a dimensionless quantity, $s = \delta B/\bar{d}$, where δB is the space between any two adjacent levels and $\bar{d} = 1/\bar{\rho}$ is the mean level spacing. Whereas the nearest-neighbour spacing (NNS) distribution $P(s)$ of non-interacting levels is Poissonian, $P_P = \exp(-s)$, strongly interacting levels obey a totally different distribution, which, in the case of GOE statistics, is known as the Wigner–Dyson (W–D) distribution, or 'Wigner surmise'[26]

$$P_{WD} = \frac{\pi}{2} s \exp\left(-\frac{\pi}{4} s^2\right) \quad (1)$$

which shows a strong level repulsion for small s: $P_{WD}(0) = 0$. The field of application of the W–D distribution is so vast as to make it a universal feature of very complex systems, such as heavy nuclei, disordered conductors, zeros of the Riemann function in number theory, and even risk management models in finance[5,8]. Remarkably, the Bohigas–Giannoni–Schmit conjecture further enriched the field of applications of GOE statistics[6,27], showing that it applies generally to chaotic systems, such as Rydberg atoms in strong magnetic fields and Sinai billiards, where only a few degrees of freedom are relevant but where motion in these degrees of freedom occurs on a highly anisotropic potential energy surface[7]. Recently, it has been speculated that even cold and ultracold atom–molecule collisions will show essential features of GOE statistics[3,4].

Inspired by these works, we statistically analyse both the experimental and calculated Fano–Feshbach spectrum according to RMT. To obtain the NNS distribution of resonances, we first derive $\bar{\rho}$ and the mean spacing between resonances, $\bar{d}$, by constructing the 'staircase function'[7]. This step-like function counts the number of resonances below a magnetic field value B and is defined as $\mathcal{N}(B) = \int_0^B \mathrm{d}B' \sum_i \delta(B' - B_i)$, where δ is the delta function and B_i is the position of the ith resonance. For our experimental data (Fig. 3a), the staircase function shows an increase of the number of resonances with B, which is linear for large B and flattens out towards lower magnetic field values (Fig. 3b). The density of resonances is given by the derivative of the staircase function. We evaluate $\bar{\rho}$ in the region above 30 G, where the staircase function shows a linear relationship (Methods), and we obtain $\bar{\rho} = 3.0(3)\ \mathrm{G}^{-1}$ and $\bar{d} = 0.33(3)$ G. We perform a similar analysis with ^{166}Er and find that $\bar{\rho} = 3.3(3)\ \mathrm{G}^{-1}$ and that $\bar{d} = 0.31(3)$ G (Extended Data Fig. 3). For data from coupled-channel calculations, we find that $\bar{\rho} = 1.5\ \mathrm{G}^{-1}$ for $L_{max} = 20$ (Fig. 2). Finally, we derive the NNS distribution for the experimental and coupled-channel data by constructing a histogram of resonance spacings. We choose a number of bins of the order of $\sqrt{N}$, with N being the number of Fano–Feshbach resonances used for analysis[28]. We then rescale the histogram in terms of s and normalize the distribution to obtain $P(s)$.

Figure 4 is the main result of our statistical analysis for ^{168}Er. The plot shows the NNS distribution of the experimental and coupled-channel Fano–Feshbach resonances, together with the parameter-free Poisson and W–D distributions (equation (1)). We see an impressive agreement between the experimental result and the coupled-channel calculations. Remarkably, both follow a distribution much closer to the W–D one than to the Poissonian one. To quantify the agreement with the GOE statistics, we evaluate the reduced χ^2 statistic, $\tilde{\chi}^2$, between our data and the Poisson and W–D distributions. We find that $\tilde{\chi}^2_{WD} = 0.9$ and $\tilde{\chi}^2_P = 2.3$ for our experimental data and that $\tilde{\chi}^2_{WD} = 0.8$ and $\tilde{\chi}^2_P = 3.0$ for the data of the coupled-channel calculations. The fact that $\tilde{\chi}^2_{WD} \leq 1$ confirms that our data are well described by a W–D distribution. Similar results are found for ^{166}Er (Extended Data Fig. 4).

To investigate the spectral correlations further, we analyse our data in terms of other statistical quantities, such as the number variance and the two-gap distribution function[29] (Methods). The number variance, $\Sigma^2(\Delta B)$, measures the fluctuations in the number of resonances in a magnetic field interval ΔB (ref. 7; Methods). For uncorrelated (Poisson-distributed) levels, $\Sigma^2 = \Delta B$, indicating large fluctuations around a mean value. For quantum chaotic systems, the correlations are strong and the fluctuations are thus less spread out. In this case, $\Sigma^2 \propto \ln(\Delta B)$. This slower increase of the number variance is regarded as indicating the strong 'spectral rigidity' of the system[7]. Our observations clearly

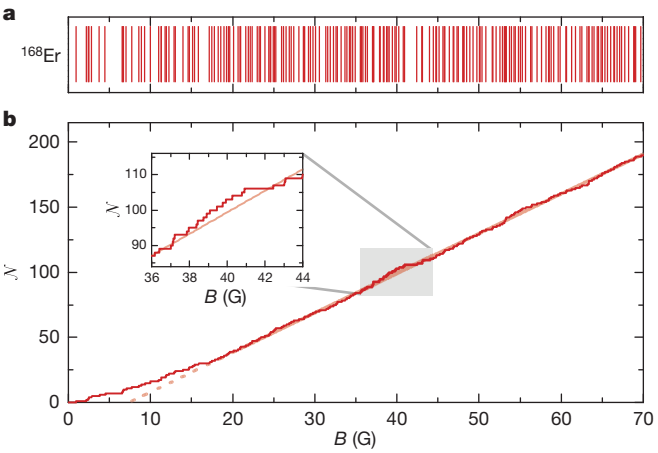

Figure 3 | Loss-maxima position and staircase function for ^{168}Er. **a**, Positions of the measured loss maxima of Fig. 1 are shown as vertical lines. **b**, The staircase function shows a linear dependence on the magnetic field at large values. A linear fit to the data above 30 G is plotted in a lighter colour. Inset, magnification of the data to emphasize the step-like nature of the staircase function.

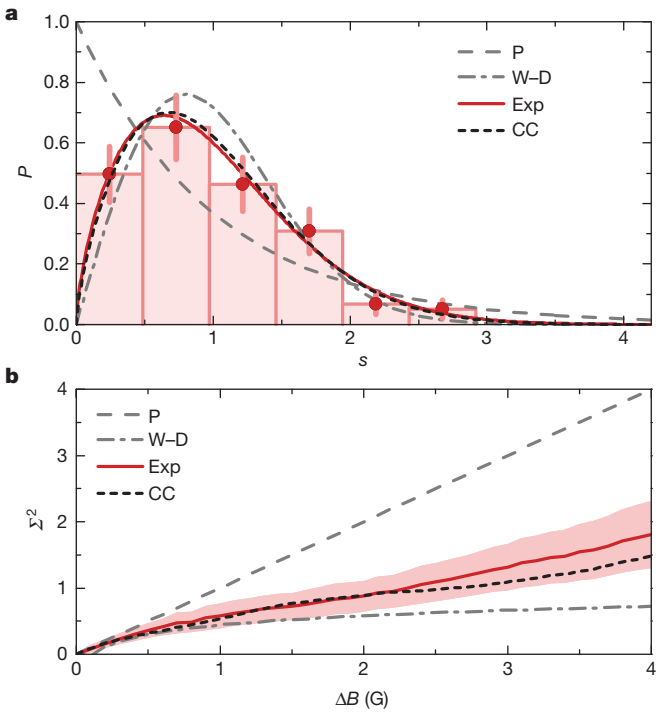

Figure 4 | NNS distribution and number variance. a, ^{168}Er NNS distribution above 30 G with a bin size of 160 mG. The plot shows the experimental data (circles) with the corresponding Brody distribution (which interpolates between Poisson and Wigner-Dyson distributions) (solid line), the Brody distribution for the coupled-channel calculation with $L_{max} = 20$ (short-dashed line), and the parameter-free distributions P_P (long-dashed line) and P_{WD} (dash–dot line). The Brody distribution is given in Methods. For the error bars in the experimental data, we assume a Poisson counting error. **b**, Number variances for the experimental data (solid line) with a 2σ confidence band (shaded area), the coupled-channel data (short-dashed line), P_P (long-dashed line) and P_{WD} (dash–dot line).

deviate from the Poissonian behaviour, showing that Σ^2 tends to the W–D case (Fig. 4b), and confirm the presence of correlations in our system.

Our observations reproduce the salient features predicted by GOE statistics for chaotic systems, the level repulsion and the spectral rigidity. This implies a degree of complexity in Er + Er cold collisions unprecedented in any previous ultracold scattering system. Our results bring the powerful analytical tools of quantum chaos to bear[7]. In particular, these approaches connect the large-scale structure of the spectra to simple features such as the shortest closed classical orbits in the potential energy surface, where these connections are made by the Gutzwiller trace formula[30]. Identifying the most important closed orbits will then shed light on the potential energy surface itself, providing a route to describing ultracold collisions that is complementary to the elaborate close-coupling calculations, which will be difficult to connect in detail with the data.

Erbium systems are the first in which statistical analyses and chaotic behaviour are important to ultracold collisions, but they will not be the last. Specifically, much experimental effort is being exerted on producing ultracold molecular samples, which also have highly anisotropic potential energy surfaces. Learning to understand complex spectra, by acknowledging their essentially chaotic nature, represents a turning point in how the field will consider ultracold collisions in future and provides new inroads into ultracold chemistry.

METHODS SUMMARY

For bosonic sample preparation, we follow the approach of ref. 12. We obtain about 3×10^5 optically trapped atoms at a density of 3×10^{13} cm^{-3}. The trap-loss spectroscopy is performed in a trap with frequencies of $(\nu_x, \nu_y, \nu_z) = (65, 26, 270)$ Hz. The temperature of the cloud is measured by time-of-flight imaging at 0.4 G, which yields $T_{168} = 326(4)$ nK for ^{168}Er and $T_{166} = 415(4)$ nK for ^{166}Er. We ramp the magnetic field to a probe value between 0 and 70 G within 10 ms, and hold the atomic cloud in the optical dipole trap for 400 ms. We observe an increase in the temperature to 560 nK at a magnetic field of about 50 G due to the ramping over many Fano–Feshbach resonances. For fermionic sample preparation, we follow the approach of ref. 13. We obtain about 1.2×10^5 fermionic atoms at a density of 2×10^{14} cm^{-3} and at a temperature of $0.4T_F$, where $T_F = 1.0(1)$ μK is the Fermi temperature. The trap frequencies are $(\nu_x, \nu_y, \nu_z) = (427, 66, 457)$ Hz.

Online Content Any additional Methods, Extended Data display items and Source Data are available in the online version of the paper; references unique to these sections appear only in the online paper.

Received 6 December 2013; accepted 6 February 2014.
Published online 12 March 2014.

1. Inouye, S. *et al.* Observation of Feshbach resonances in a Bose–Einstein condensate. *Nature* **392,** 151–154 (1998).
2. Chin, C., Grimm, R., Julienne, P. S. & Tiesinga, E. Feshbach resonances in ultracold gases. *Rev. Mod. Phys.* **82,** 1225–1286 (2010).
3. Mayle, M., Ruzic, B. P. & Bohn, J. L. Statistical aspects of ultracold resonant scattering. *Phys. Rev. A* **85,** 062712 (2012).
4. Mayle, M., Quéméner, G., Ruzic, B. P. & Bohn, J. L. Scattering of ultracold molecules in the highly resonant regime. *Phys. Rev. A* **87,** 012709 (2013).
5. Guhr, T., Müller-Groeling, A. & Weidenmüller, H. A. Random-matrix theories in quantum physics: common concepts. *Phys. Rep.* **299,** 189–425 (1998).
6. Bohigas, O., Giannoni, M. J. & Schmit, C. Characterization of chaotic quantum spectra and universality of level fluctuation laws. *Phys. Rev. Lett.* **52,** 1–4 (1984).
7. Weidenmüller, H. A. & Mitchell, G. E. Random matrices and chaos in nuclear physics: nuclear structure. *Rev. Mod. Phys.* **81,** 539–589 (2009).
8. Mitchell, G. E., Richter, A. & Weidenmüller, H. A. Random matrices and chaos in nuclear physics: nuclear reactions. *Rev. Mod. Phys.* **82,** 2845–2901 (2010).
9. Brody, T. A. A statistical measure for the repulsion of energy levels. *Lett. N. Cim. Ser. 2* **7,** 482–484 (1973).
10. Lu, M., Burdick, N. Q., Youn, S. H. & Lev, B. L. Strongly dipolar Bose-Einstein condensate of dysprosium. *Phys. Rev. Lett.* **107,** 190401 (2011).
11. Lu, M., Burdick, N. Q. & Lev, B. L. Quantum degenerate dipolar Fermi gas. *Phys. Rev. Lett.* **108,** 215301 (2012).
12. Aikawa, K. *et al.* Bose-Einstein condensation of erbium. *Phys. Rev. Lett.* **108,** 210401 (2012).
13. Aikawa, K. *et al.* Reaching Fermi degeneracy via universal dipolar scattering. *Phys. Rev. Lett.* **112,** 010404 (2014).
14. Hancox, C. I., Doret, S. C., Hummon, M. T., Luo, L. & Doyle, J. M. Magnetic trapping of rare-earth atoms at millikelvin temperatures. *Nature* **431,** 281–284 (2004).
15. Connolly, C. B., Au, Y. S., Doret, S. C., Ketterle, W. & Doyle, J. M. Large spin relaxation rates in trapped submerged-shell atoms. *Phys. Rev. A* **81,** 010702 (2010).
16. Kokoouline, V., Santra, R. & Greene, C. H. Multichannel cold collisions between metastable Sr atoms. *Phys. Rev. Lett.* **90,** 253201 (2003).
17. Krems, R. V., Groenenboom, G. C. & Dalgarno, A. Electronic interaction anisotropy between atoms in arbitrary angular momentum states. *J. Phys. Chem. A* **108,** 8941–8948 (2004).
18. Petrov, A., Tiesinga, E. & Kotochigova, S. Anisotropy-induced Feshbach resonances in a quantum dipolar gas of highly magnetic atoms. *Phys. Rev. Lett.* **109,** 103002 (2012).
19. Berninger, M. *et al.* Feshbach resonances, weakly bound molecular states, and coupled-channel potentials for cesium at high magnetic fields. *Phys. Rev. A* **87,** 032517 (2013).
20. Takekoshi, T. *et al.* Towards the production of ultracold ground-state RbCs molecules: Feshbach resonances, weakly bound states, and the coupled-channel model. *Phys. Rev. A* **85,** 032506 (2012).
21. Kotochigova, S., Levine, H. & Tupitsyn, I. Correlated relativistic calculation of the giant resonance in the Gd^{3+} absorption spectrum. *Int. J. Quantum Chem.* **65,** 575–584 (1997).
22. Kramida, A. *et al.* NIST Atomic Spectra Database Version 5.0. http://www.nist.gov/pml/data/asd.cfm (2013).
23. Lawler, J. E., Wyart, J. & Den Hartog, E. A. Atomic transition probabilities of Er I. *J. Phys. At. Mol. Opt. Phys.* **43,** 235001 (2010).
24. Gao, B. Zero-energy bound or quasibound states and their implications for diatomic systems with an asymptotic van der Waals interaction. *Phys. Rev. A* **62,** 050702(R) (2000).
25. Wigner, E. P. On a class of analytic functions from the quantum theory of collisions. *Ann. Math.* **53,** 36–67 (1951).
26. Dyson, F. J. & Mehta, M. L. Statistical theory of the energy levels of complex systems. IV. *J. Math. Phys.* **4,** 701–712 (1963).
27. Alt, H. *et al.* Gaussian orthogonal ensemble statistics in a microwave stadium billiard with chaotic dynamics: Porter-Thomas distribution and algebraic decay of time correlations. *Phys. Rev. Lett.* **74,** 62–65 (1995).
28. Taylor, J. *An Introduction to Error Analysis: The Study of Uncertainties in Physical Measurements* 272 (Univ. Science Books, 1997).
29. Brody, T. A. *et al.* Random-matrix physics: spectrum and strength fluctuations. *Rev. Mod. Phys.* **53,** 385–479 (1981).

30. Gutzwiller, M. *Chaos in Classical and Quantum Mechanics* (Springer, 1990).

Acknowledgements The Innsbruck group thanks R. Grimm for discussions and S. Baier, C. Ravensbergen and M. Brownnutt for reading the manuscript. S.K. and A.P. thank E. Tiesinga for discussions. J.L.B. is supported by an ARO MURI. The Innsbruck team is supported by the Austrian Science Fund (FWF) through a START grant under project no. Y479-N20 and by the European Research Council under project no. 259435. K.A. is supported within the Lise-Meitner program of the FWF. Research at Temple University is supported by AFOSR and NSF PHY-1308573.

Author Contributions A.F., M.M., K.A. and F.F. did the experimental work and statistical analysis of the data. C.M., A.P. and S.K. did the theoretical work on coupled-channel calculations and RQDT. J.L.B. did the theoretical work on RMT. The manuscript was written with substantial contributions from all authors.

Author Information Reprints and permissions information is available at www.nature.com/reprints. The authors declare no competing financial interests. Readers are welcome to comment on the online version of the paper. Correspondence and requests for materials should be addressed to F.F. (francesca.ferlaino@uibk.ac.at).

METHODS

Experimental procedures. For bosonic sample preparation, we follow the approach of ref. 12. In brief, after the magneto-optical trap[31], we load the atoms in an optical dipole trap composed of two laser beams in the horizontal (1,064 nm, 0.4 W, single mode) and vertical (1,064 nm, 4.0 W, broadband Yb fibre laser) directions. In the trap, we force evaporation by ramping down the power of both trapping laser beams within 6.2 s, in the presence of a homogeneous magnetic field of 0.4 G to prevent spin flips to other Zeeman states. We stop evaporative cooling before the onset of Bose–Einstein condensation. Our final trap has frequencies of $(\nu_x, \nu_y, \nu_z) = (65, 26, 270)$ Hz and contains about 3×10^5 atoms at a density of 3×10^{13} cm^{-3}. The temperature of the atomic cloud is measured by time-of-flight imaging for both isotopes at 0.4 G, which gives $T_{168} = 326(4)$ nK and $T_{166} = 415(4)$ nK. We ramp the homogeneous magnetic probe field up to 70 G within 10 ms and hold the atomic cloud in the optical dipole trap for 400 ms. The magnetic field is suddenly (<5 ms, limited by eddy currents) switched off and the atom number and cloud size are measured via absorption imaging after a time of flight of 15 ms. We observe an increase in temperature to 560 nK in a magnetic field of about 50 G due to ramping over many Fano–Feshbach resonances. For fermionic sample preparation, we follow the approach of ref. 13. We obtain about 1.2×10^5 fermionic atoms at a density of 2×10^{14} cm^{-3} and at a temperature of $0.4T_F$, where $T_F = 1.0(1)$ μK is the Fermi temperature. The trap frequencies are (427, 66, 457) Hz.

Magnetic field control. An analogue feedback loop stabilizes the current for the homogeneous magnetic field coils with a relative short-term stability of better than 2×10^{-4}. Calibration of the magnetic field is done by driving a radio-frequency transition between Zeeman states $m_J = -6$ and $m_J = -5$. Trap-loss spectroscopy is carried out in steps of 20 mG (out of resonance) and 5 mG (on resonance). The long-term offset stability of the magnetic field was observed during the data recording period to be better than 4 mG within one week.

Coupled-channel calculations. We perform exact coupled-channel calculations for Er + Er scattering in the basis $|j_1 m_{J,1}, j_2 m_{J,2}, \ell m_\ell\rangle \equiv Y_{\ell m_\ell}(\theta,\phi)|j_1 m_{J,1}\rangle|j_2 m_{J,2}\rangle$, where $j_{a=1,2}$ are the atomic vector angular momenta with space-fixed projections $m_{J,a=1,2}$ along the magnetic field direction, and the spherical harmonics $Y_{\ell m_\ell}(\theta,\phi)$ describe molecular rotation with partial-wave quantum numbers ℓ and m_ℓ. The angles θ and ϕ orient the internuclear axis relative to the magnetic field.

For a closed-coupling calculation of the rovibrational motion and the scattering of atoms, we need all the electronic potentials dissociating to the threshold of two ground-state atoms. The total number of B–O potentials is determined by the vector $J = j_1 + j_2$ and its projection along the internuclear axis, Ω. For each value of Ω, there are $(2J + 1) - \Omega$ B–O potentials, with $J = 6$ in the case of Er. This gives a total of 91 B–O potentials for Er_2, of which 49 are gerade potentials and 42 are ungerade. For collisions of bosons in the same Zeeman state, only even states matter. These potential surfaces have been obtained using an *ab initio* relativistic, multi-reference configuration–interaction method[21], and converted into a tensor operator form with R-dependent coefficients. Examples of tensor operators are the exchange interaction, $V_{ex}(R) j_1 \bullet j_2$ and the anisotropic quadrupole-rotation operator $V_Q(R) Y_2(\hat{R}) \bullet [j_1 \otimes j_1]_2$ coupling the quadrupole operator, $[j_1 \otimes j_1]_2$, of one atom with angular momentum j_1 to the rotation of the molecule. See ref. 18 for other operators.

Collisions of submerged 4*f*-shell atoms at low temperatures also depend on the intermediate/long-range isotropic and anisotropic dispersion and magnetic dipole–dipole and quadrupole–quadrupole interatomic interactions. The van der Waals dispersion potentials for two ground-state atoms are obtained using the transition frequencies and oscillator strengths[22,23]. The quadrupole moment of Er is calculated using an unrestricted atomic coupled-cluster method with single, double and perturbative triple excitations[32] (UCCSD(T)) and is shown to be small at $Q = 0.029$ a.u.

We use a first-principle coupled-channel model to calculate anisotropy-induced magnetic Fano–Feshbach resonance spectra of bosonic Er. The model treats the Zeeman, magnetic dipole–dipole, and isotropic and anisotropic dispersion interactions on equal footing. The Hamiltonian includes

$$H = -\frac{\hbar^2}{2\mu}\frac{\mathrm{d}^2}{\mathrm{d}R^2} + \frac{\ell \bullet \ell}{2\mu R^2} + H_Z + V(R,\tau)$$

where vector R describes the orientation of and separation between the two atoms. The first two terms are the radial kinetic and rotational energy operators, respectively. The Zeeman interaction is $H_Z = g\mu_B(j_{1z} + j_{2z})B$, where g is the atomic g-factor and j_{iz} is the z component of the angular momentum operator j_i of atom $i = 1, 2$. The interaction, $V(R,\tau)$, includes the B–O and magnetic dipole–dipole interaction potentials, which are anisotropic, and τ labels the electronic variables. Finally, μ is the reduced mass and $V(R,\tau) \to 0$ as $R \to \infty$. Coupling between the basis states is due to $V(R,\tau)$, inducing either isotropic (ℓ and m_ℓ conserving) or anisotropic (ℓ or m_ℓ changing) couplings. The Hamiltonian conserves $M_{tot} = m_{J,1} + m_{J,2} + m_\ell$ and is invariant under the parity operation so that only even-ℓ or odd-ℓ partial waves are coupled. In the atomic basis set, the Zeeman and rotational interactions are diagonal.

Staircase function and density of resonances. The density of resonances is evaluated as the derivative of the staircase function. Because we observe a nonlinear behaviour of the staircase function at low magnetic field values, we perform a more careful analysis of the data. For calculating the density of resonances we take the slope of a linear fit to the staircase function within an interval of 10 G. This fitting interval is then moved across the magnetic field axis, to get an averaged value of the density of resonances at each position (Extended Data Fig. 5). The size of the interval is chosen such that the density of resonances can be evaluated reliably. Larger values for the size of this interval will give values for the density of resonances that are too strongly averaged, and an underlying structure will not be visible any more. Smaller values tend to increase the noise in the density of resonances, owing to the step-like nature of $\mathcal{N}(B)$. We calculate the arithmetic mean and standard deviation for values above 30 G and get a density of resonances for the two isotopes of $\bar{\rho}_{168} = 3.0(3)$ G^{-1} and $\bar{\rho}_{166} = 3.3(3)$ G^{-1}.

NNS probability distribution. Because the density of resonances is not constant below 30 G, we restrict our analysis to resonances appearing from 30 to 70 G. We plot a histogram of spacings between adjacent resonances given by $d_i = B_{i+1} - B_i$. For this an appropriate number of bins is chosen, of the order of $\sqrt{N}$, with N being the total number of Fano–Feshbach resonances observed up to 70 G. This ensures a bin size at least an order of magnitude larger than the mean resolution of the trap-loss spectroscopy scan. For every bin, a statistical counting error according to a Poisson distribution is assigned. Next, the magnetic field is divided by the mean spacing of resonances to get the dimensionless quantity $s = B/\bar{d}$. To calculate the NNS probability distribution, $P(s)$, the histogram has to be normalized such that $\int_0^\infty \mathrm{d}s\, P(s) = 1$. As shown in ref. 29, the probability distribution of uncorrelated random numbers is simply given by the Poisson distribution $P_P(s) = \exp(-s)$. A theoretical spacing distribution of random matrices cannot be written in a simple form but, according to the Wigner surmise, an excellent approximation is given by the W–D distribution, $P_{WD}(s) = (\pi s/2)\exp(-\pi s^2/4)$. A way of discriminating between these two distributions is to fit the 'Brody distribution' to the NNS distribution[9]. It is an empirical function with a single fitting parameter, η, which interpolates between P_{WD} and P_P and quantifies the tendency (and not the degree of chaoticity) of the observed distribution to be more Poisson-like ($\eta = 0$) or more W–D-like ($\eta = 1$). It is defined by

$$P_B(s) = A s^\eta \exp(-\alpha s^{\eta+1})$$
$$A = (\eta + 1)\alpha$$
$$\alpha = \Gamma\left(\frac{\eta+2}{\eta+1}\right)^{\eta+1}$$

where Γ denotes the Gamma function. From a least-squares fit to the experimental data, we obtain $\eta_{168} = 0.66(10)$ for ^{168}Er and $\eta_{166} = 0.73(18)$ for ^{166}Er, and a fit to the coupled-channel data gives $\eta_{CC} = 0.72(18)$.

Number variance. The number variance, Σ^2, is a quantity that depends on long-range correlations between resonance spacings within an interval ΔB. It is defined by

$$\Sigma^2(\Delta B) = \overline{n^2(B_0,\Delta B)} - \overline{n(B_0,\Delta B)}^2$$

where $n(B_0,\Delta B) = \mathcal{N}(B_0 + \Delta B) - \mathcal{N}(B_0)$ is the number of resonances in the interval $[B_0, B_0 + \Delta B]$ and the bar denotes the mean value over all B_0. For a Poisson distribution, $\Sigma^2 = \Delta B$. By contrast, for a spectrum according to RMT we expect that $\Sigma^2 = (2/\pi^2)[\ln(2\pi\Delta B) + \gamma + 1 - \pi^2/8]$ for large ΔB, where $\gamma = 0.5772\ldots$ is Euler's constant[26]. This behaviour reflects that there are only very small fluctuations around an average number of resonances within a given interval of size ΔB (spectral rigidity). Compared with the NNS distribution, the number variance is more suitable to probing long distances in the spectrum. A clear signature of level repulsion on the one hand and a large spectral rigidity on the other are central properties of strong correlations between levels according to RMT[29].

Two-gap distribution function. In addition to analysing the NNS distribution, we use a second method for testing whether the observed distribution of Fano–Feshbach resonances obeys RMT. To plot the NNS distribution, we have to make sure that the staircase function increases linearly over large ranges. This we have ensured in our statistical analysis by considering only data above 30 G. If the staircase function does not increase in a linear manner over a large region, an unfolding procedure has to be carried out before further analysis[29]. Because the statistical analysis is very sensitive to the unfolding procedure and there is no clear definition of how it should be carried out[7], the use of an unfolding procedure makes the statistical analysis error-prone.

To circumvent this problem, an unfolding-independent method was developed in refs 33, 34. This method consists of calculating the ratio of two consecutive gaps between resonances. The 'two-gap correlation function' is defined by

$$0 \leq r_i = \frac{\min(d_i, d_{i-1})}{\max(d_i, d_{i-1})} \leq 1$$

with d_i the spacing between two neighbouring resonances. As long as the density of resonances does not vary on the scale of the mean level spacing, an unfolding procedure is not needed for calculating this quantity. A Poisson distribution of resonances shows a two-gap correlation distribution following $P(r) = 2/(1+r)^2$, with a mean value of $\langle r \rangle_{\mathrm{P}} = 2\ln(2) - 1 \approx 0.386$. In contrast, the mean value of a W–D distribution[34] can be calculated to be $\langle r \rangle_{\mathrm{WD}} \approx 0.53(1)$. By using the mean values of both distributions, we can introduce a quantity η_r, which quantifies the proximity to either a Poisson distribution ($\eta_r = 0$) or a W–D distribution ($\eta_r = 1$):

$$\eta_r = \frac{\langle r \rangle - \langle r \rangle_{\mathrm{P}}}{\langle r \rangle_{\mathrm{WD}} - \langle r \rangle_{\mathrm{P}}}$$

For the experimental data set from 30 to 70 G, we find values of $\langle r \rangle_{168} = 0.51(4)$ for ^{168}Er and values of $\langle r \rangle_{166} = 0.49(4)$ for ^{166}Er. These results give values of $\eta_r^{168} = 0.8(2)$ and $\eta_r^{166} = 0.7(2)$, respectively, and are in good agreement with the fitting results of the NNS distribution using the Brody distribution. A Fano–Feshbach resonance distribution according to RMT can thus be supported by this second method as well.

31. Frisch, A. *et al.* Narrow-line magneto-optical trap for erbium. *Phys. Rev. A* **85,** 051401 (2012).
32. Watts, J. D., Gauss, J. & Bartlett, R. J. Coupled-cluster methods with noniterative triple excitations for restricted open-shell Hartree-Fock and other general single determinant reference functions: energies and analytical gradients. *J. Chem. Phys.* **98,** 8718 (1993).
33. Oganesyan, V. & Huse, D. A. Localization of interacting fermions at high temperature. *Phys. Rev. B* **75,** 155111 (2007).
34. Kollath, C., Roux, G., Biroli, G. & Läuchli, A. M. Statistical properties of the spectrum of the extended Bose-Hubbard model. *J. Stat. Mech.* **2010,** P08011 (2010).

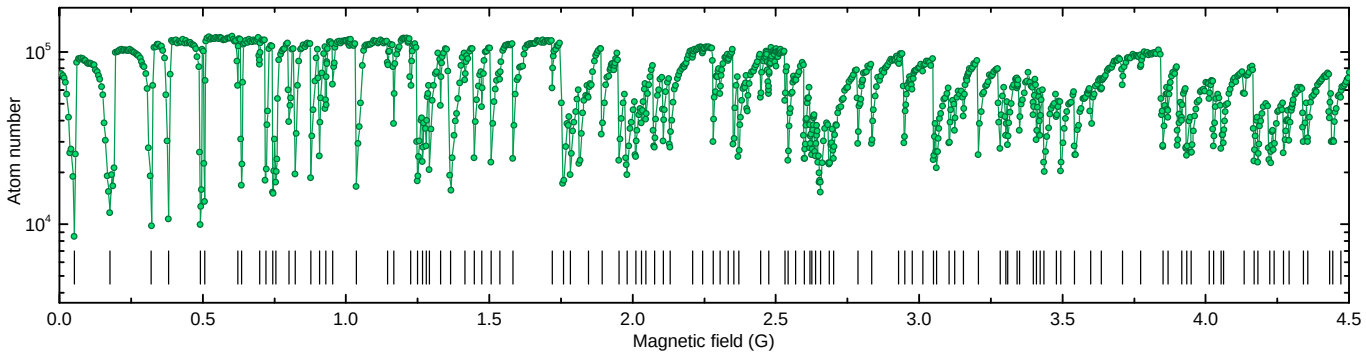

Extended Data Figure 1 | Fano–Feshbach spectrum of fermionic ^{167}Er from 0 to 4.5 G. The trap-loss spectroscopy is performed in an optically trapped sample of fermionic Er atoms at a temperature of $0.4T_F$, where $T_F = 1.0(1)$ μK is the Fermi temperature. The atoms are spin-polarized in the lowest Zeeman sublevel, $m_F = -19/2$. We keep the atomic sample at the magnetic probing field for a holding time of 100 ms. We observe 115 resonances up to 4.5 G, which we take to be Fano–Feshbach resonances between identical fermions. The corresponding mean density is about 26 resonances per gauss.

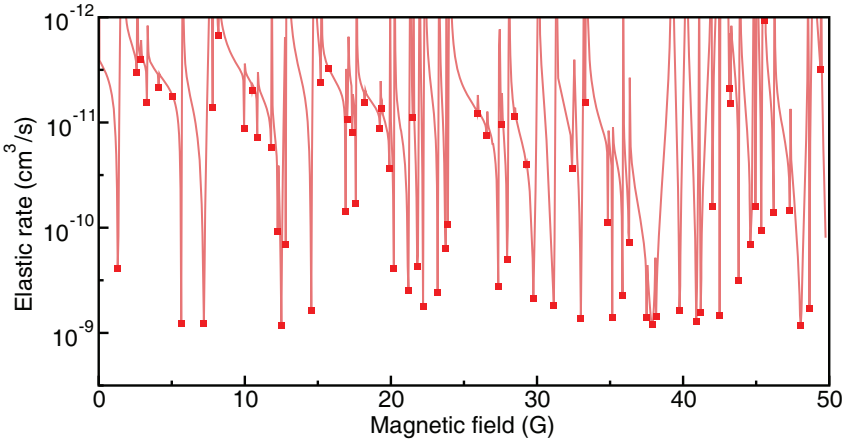

Extended Data Figure 2 | Elastic rate coefficient of $m_J = -6$ ^{168}Er collisions. The *s*-wave elastic rate coefficient as a function of magnetic field assuming a collision energy of $E = k_B \times (360\,\mathrm{nK})$. Partial waves up to $\ell = 20$ are included. A divergence of the elastic rate coefficient, that is, the position of a Fano–Feshbach resonance, is marked with squares.

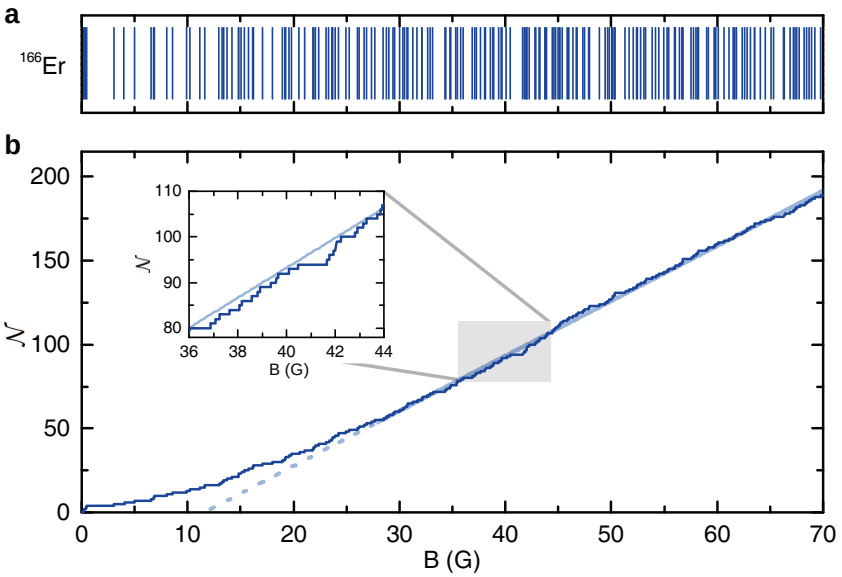

Extended Data Figure 3 | Statistical analysis of high-density Fano–Feshbach resonances of isotope ^{166}Er. **a**, Positions of the resonances are marked with vertical lines. **b**, The staircase function shows a similar behaviour to ^{168}Er (Fig. 3). A linear fit to the data above 30 G is plotted in a lighter colour. From the staircase function, we calculate a mean density of resonances of $\bar{\rho} = 3.3(3)\ \mathrm{G}^{-1}$, which corresponds to a mean distance between resonances of $\bar{d} = 0.31(3)$ G.

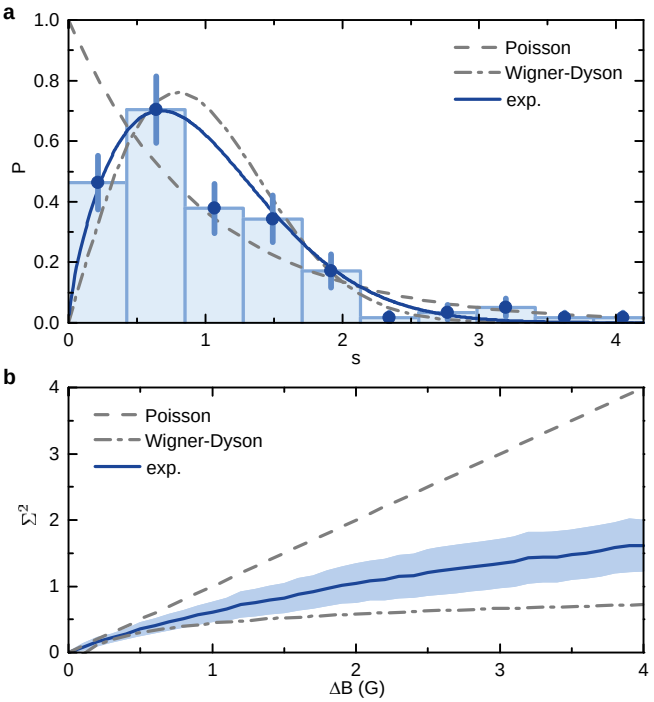

Extended Data Figure 4 | NNS distribution and number variance. **a**, ^{168}Er NNS distribution above 30 G with a bin size of 140 mG. For the error bars we assume a Poisson counting error. The plot shows the experimental data (circles) with the corresponding Brody distribution (solid line). The parameter-free distributions P_P (dashed line) and P_{WD} (dash–dot line) are shown, and $\tilde{\chi}^2_P = 2.32$ for the Poisson distribution and $\tilde{\chi}^2_{WD} = 1.85$ for the W–D distribution. **b**, Number variance, Σ^2, for the same experimental data (solid line) with a 2σ confidence band (shaded area). The number variance of the experimental data shows a clear deviation from the number variance of a Poisson distribution.

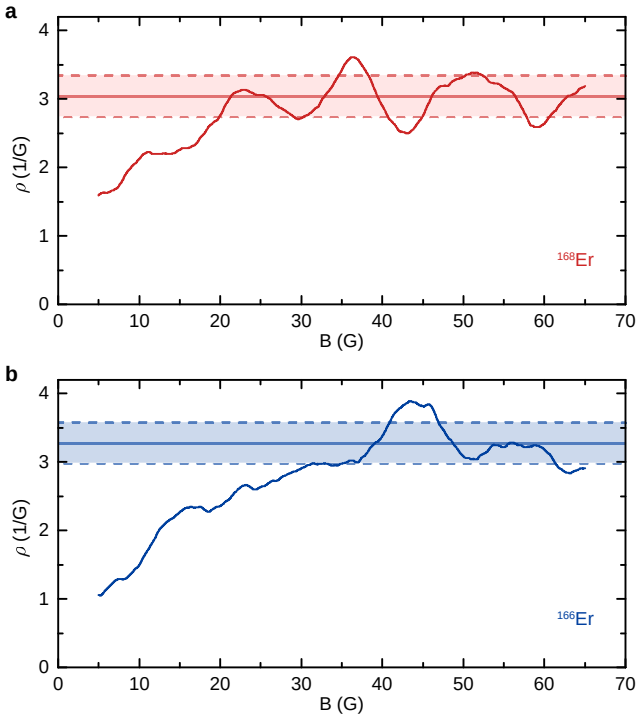

Extended Data Figure 5 | Density of resonances as a function of the magnetic field. The densities of resonances for ^{168}Er (**a**) and ^{166}Er (**b**) are given as an averaged derivative of the staircase function (dark solid lines) using an averaging region 10 G in size. At small magnetic field values, the density of resonances is about 1.5 G^{-1}, and it increases with the magnetic field up to about 30 G. For larger magnetic fields, the density is roughly constant. The staircase function also suggests this behaviour. From the data above 30 G, we calculate the mean value (light solid lines) and the standard deviation (light dotted lines) of the density of resonances.

Extended Data Table 1 | Fano–Feshbach resonances data for isotope ^{168}Er

i	B (G)	Δ (mG)	meth.
1	0.912(1)	39(2)	Z
2	2.167(1)	36(1)	Z
3	2.436(3)	14(9)	G
4	2.476(1)	153(6)	G
5	2.838(9)	16(2)	G
6	3.778(1)	22(2)	G
7	4.481(1)	23(2)	G
8	6.558(1)	29(5)	G
9	6.594(1)	22(9)	G
10	6.674(5)	217(10)	Z
11	7.048(5)	343(8)	Z
12	7.725(1)	15(2)	G
13	8.549(7)	900(16)	Z
14	8.909(1)	18(2)	G
15	9.311(1)	13(2)	G
16	9.946(1)	18(2)	G
17	11.004(1)	17(1)	G
18	11.274(1)	17(1)	G
19	11.329(1)	11(1)	G
20	11.807(1)	22(1)	G
21	11.913(1)	18(1)	G
22	12.250(1)	18(1)	G
23	12.873(1)	11(1)	G
24	13.029(1)	15(1)	G
25	13.968(1)	16(1)	G
26	14.614(1)	20(1)	G
27	14.711(1)	14(1)	G
28	15.126(1)	14(1)	G
29	15.336(1)	19(1)	G
30	15.851(1)	11(1)	G
31	17.180(1)	23(1)	G
32	17.450(1)	21(2)	G
33	17.808(3)	207(4)	Z
34	18.229(1)	18(1)	G
35	18.566(1)	19(2)	G
36	18.948(1)	20(1)	G
37	19.258(1)	21(2)	G
38	19.469(1)	145(1)	Z
39	19.66(1)	171(13)	Z
40	20.138(1)	16(1)	G
41	20.627(1)	18(2)	G
42	20.884(1)	20(2)	G
43	20.965(1)	25(2)	Z
44	21.588(1)	47(2)	Z
45	21.934(1)	43(2)	Z
46	22.146(1)	16(1)	G
47	22.34(1)	190(13)	Z
48	22.960(1)	159(2)	Z
49	23.224(1)	21(1)	G
50	23.413(1)	21(2)	G
51	23.953(1)	67(3)	Z
52	24.40(2)	48(15)	Z
53	24.549(1)	73(3)	Z
54	24.649(1)	14(3)	G
55	24.908(2)	100(5)	Z
56	25.117(1)	42(3)	Z
57	25.265(1)	17(2)	G
58	25.925(1)	26(3)	G
59	26.202(1)	12(1)	G
60	26.534(1)	19(1)	G
61	26.877(1)	99(4)	Z
62	27.098(1)	18(1)	G
63	27.447(1)	20(1)	G
64	28.070(1)	23(1)	G
65	28.643(1)	21(3)	G
66	28.737(1)	19(1)	G
67	29.233(1)	17(1)	G
68	29.448(1)	32(2)	Z
69	29.797(1)	25(2)	Z
70	30.057(1)	26(2)	G
71	30.541(1)	15(1)	Z
72	31.369(1)	19(2)	G
73	31.602(1)	18(1)	G
74	31.903(1)	16(2)	G
75	32.243(1)	25(2)	Z
76	32.556(1)	25(2)	G
77	32.753(2)	283(5)	Z
78	33.245(1)	17(1)	G
79	33.703(1)	21(1)	G
80	33.903(1)	61(2)	Z
81	34.206(1)	13(1)	G
82	34.340(1)	21(1)	G
83	34.647(1)	16(1)	G
84	34.939(1)	53(1)	Z
85	35.524(1)	17(2)	Z
86	35.713(1)	45(1)	Z
87	35.836(1)	15(1)	G
88	36.148(1)	132(4)	Z
89	36.399(1)	13(3)	G
90	37.015(1)	83(1)	Z
91	37.105(1)	4(1)	G
92	37.137(1)	17(2)	G
93	37.198(1)	54(2)	Z
94	37.856(1)	178(24)	G
95	37.944(1)	152(1)	Z
96	38.362(1)	17(2)	G
97	38.416(1)	18(2)	G
98	38.728(1)	19(2)	G
99	38.895(1)	23(2)	G
100	39.075(1)	16(1)	G
101	39.458(1)	16(3)	G
102	39.739(8)	1722	Z
103	39.919(1)	16(3)	G
104	40.252(6)	202(7)	Z
105	40.772(2)	106(4)	Z
106	40.901(1)	17(2)	G
107	42.429(1)	20(1)	G
108	43.019(1)	20(2)	G
109	43.078(1)	13(1)	G
110	43.969(1)	23(1)	Z
111	44.404(1)	44(4)	G
112	44.731(1)	109(7)	Z
113	44.823(1)	18(2)	G
114	45.165(1)	27(4)	G
115	45.571(1)	156(8)	Z
116	45.772(1)	19(3)	G
117	45.851(1)	88(4)	Z
118	46.343(1)	89(3)	Z
119	46.815(1)	20(2)	G
120	46.900(1)	12(3)	G
121	47.284(3)	58(10)	G
122	47.485(7)	1193	Z
123	48.035(1)	141(7)	Z
124	48.082(1)	7(2)	G
125	48.207(1)	21(2)	G
126	48.473(1)	98(3)	Z
127	48.842(2)	138(5)	Z
128	49.251(1)	14(2)	G
129	49.735(1)	31(1)	Z
130	50.019(1)	15(3)	G
131	50.113(1)	104(4)	Z
132	50.325(1)	18(2)	G
133	50.788(1)	15(2)	G
134	51.624(1)	15(1)	G
135	51.651(1)	12(2)	G
136	52.110(1)	18(1)	G
137	52.552(2)	66(3)	Z
138	52.835(1)	14(1)	G
139	53.082(1)	13(2)	G
140	53.195(1)	33(5)	G
141	53.245(1)	14(3)	G
142	53.299(1)	33(4)	Z
143	53.738(1)	31(3)	G
144	53.925(1)	19(1)	G
145	54.272(2)	20(5)	Z
146	54.404(1)	12(1)	G
147	54.763(4)	57(4)	Z
148	55.035(1)	18(2)	G
149	55.239(1)	18(3)	G
150	55.692(1)	300	G
151	56.314(1)	109(3)	Z
152	56.436(1)	15(3)	G
153	57.06(2)	3531	Z
154	57.612()	89(1)	Z
155	58.167(2)	13(2)	Z
156	58.426(1)	14(2)	G
157	58.528(1)	7(1)	Z
158	58.795(2)	27(4)	Z
159	59.078(1)	55(2)	Z
160	59.609(1)	16(2)	G
161	59.875(3)	85(10)	Z
162	60.585(1)	51(3)	G
163	60.646(1)	8(2)	G
164	61.241(1)	22(1)	G
165	61.759(1)	13(1)	G
166	62.271(1)	15(1)	G
167	62.510(1)	52(3)	Z
168	63.174(1)	9(2)	Z
169	63.367(1)	6(2)	G
170	63.398(1)	18(3)	Z
171	63.727(1)	17(3)	G
172	63.985(3)	348(7)	Z
173	64.374(4)	76(5)	Z
174	64.522(1)	16(1)	G
175	64.889(1)	17(1)	G
176	64.985(1)	20(1)	G
177	65.302(1)	37(1)	Z
178	65.671(1)	33(3)	Z
179	65.989(1)	46(2)	Z
180	66.401(1)	58(2)	Z
181	66.475(1)	51(1)	Z
182	66.790(1)	118(3)	Z
183	67.103(1)	497	Z
184	67.354(1)	18(2)	G
185	67.767(1)	12(1)	G
186	68.240(1)	113(3)	Z
187	68.810(1)	26(1)	Z
188	68.895(1)	16(4)	G
189	69.046(1)	347(3)	Z
190	69.727(1)	19(2)	G

Fano–Feshbach resonance positions, B, and widths, Δ, of the loss maxima shown in Fig. 1. For convenience, the loss features are reported in ascending order and labelled with index i. The error in brackets is 1σ. Δ is determined either from a Gaussian fit as the half-width at $1/e^2$ (method G) or by measuring the zero crossing of the resonance, B_{zero}, being $\Delta = |B - B_{zero}|$ (method Z).

Extended Data Table 2 | Fano–Feshbach resonances data for isotope ^{166}Er

i	B (G)	Δ (mG)	meth.
1	0.121(1)	20(2)	G
2	0.244(1)	14(1)	G
3	0.366(1)	6(1)	G
4	0.490(1)	15(6)	G
5	3.056(2)	124(4)	Z
6	4.012(5)	23(1)	G
7	4.955(1)	9(2)	G
8	6.546(1)	38(2)	Z
9	6.768(1)	23(2)	G
10	6.884(1)	26(2)	G
11	8.053(1)	29(2)	G
12	8.553(1)	20(2)	G
13	9.910(1)	47(5)	Z
14	10.228(3)	116(6)	Z
15	11.108(1)	52(6)	Z
16	11.623(1)	27(1)	Z
17	12.978(1)	14(2)	G
18	13.278(1)	34(1)	Z
19	13.426(2)	92(7)	Z
20	13.686(1)	16(2)	G
21	14.177(1)	19(2)	G
22	14.801(1)	17(2)	G
23	14.835(1)	13(1)	G
24	15.077(1)	18(2)	G
25	15.371(1)	70(2)	Z
26	15.726(1)	68(2)	Z
27	16.107(1)	19(2)	G
28	16.187(1)	38(2)	Z
29	17.053(1)	25(2)	G
30	17.977(1)	17(3)	G
31	18.961(1)	20(3)	G
32	19.152(1)	22(1)	G
33	19.239()	20(1)	G
34	19.543(1)	21(3)	Z
35	19.82(1)	158(12)	Z
36	20.539(4)	417(18)	G
37	21.047(2)	63(8)	Z
38	21.803(1)	21(2)	G
39	21.922(1)	22(2)	G
40	22.068(1)	50(5)	Z
41	22.350(1)	27(2)	G
42	23.055(1)	17(2)	G
43	23.345(1)	19(2)	Z
44	23.585(1)	72(3)	G
45	23.725(1)	15(4)	G
46	23.898(1)	15(2)	G
47	24.272(1)	12(1)	G
48	24.924(1)	14(2)	G
49	25.272(1)	19(1)	G
50	26.036(1)	17(1)	G
51	26.206(1)	13(2)	G
52	26.621(1)	10(2)	G
53	26.915(1)	19(1)	G
54	27.324(1)	30(1)	Z
55	27.681(1)	23(1)	G
56	28.488(1)	31(1)	Z
57	28.726(1)	25(1)	Z
58	29.024(1)	14(1)	G
59	29.357(1)	25(1)	Z
60	29.515(1)	16(1)	G
61	30.023(1)	44(2)	Z
62	30.319(1)	21(2)	G
63	30.508(1)	31(1)	Z
64	30.703(1)	16(4)	G
65	30.810(2)	154(4)	Z
66	31.220(2)	95(10)	G
67	31.683(1)	33(2)	G
68	32.106(1)	16(2)	G
69	32.145(1)	13(2)	G
70	32.656(1)	17(2)	G
71	32.909(1)	14(2)	G
72	33.166(1)	13(2)	G
73	34.309(1)	15(1)	Z
74	34.408(1)	77(4)	Z
75	34.734(1)	19(1)	G
76	34.824(1)	13(1)	G
77	35.345(1)	15(1)	G
78	35.463(1)	18(1)	G
79	35.784(1)	14(1)	G
80	36.006(1)	18(1)	G
81	36.876(1)	14(2)	G
82	37.077(1)	49(5)	Z
83	37.253(1)	17(2)	Z
84	37.662(1)	45(3)	Z
85	38.048(1)	23(1)	G
86	38.145(1)	190(5)	Z
87	38.573(1)	39(3)	Z
88	38.788(1)	12(2)	G
89	38.888(1)	84(5)	Z
90	39.354(1)	11(2)	Z
91	39.563(2)	52(2)	Z
92	39.652(1)	110(5)	Z
93	40.099(1)	13(1)	G
94	40.459(1)	87(4)	Z
95	41.649(1)	27(1)	Z
96	41.756(1)	36(2)	Z
97	41.926(1)	17(2)	G
98	42.003(1)	18(3)	G
99	42.040(1)	14(1)	G
100	42.229(7)	473(29)	G
101	42.817(1)	53(4)	G
102	42.906(1)	19	G
103	43.146(1)	14(1)	G
104	43.273(1)	14(1)	G
105	43.716(1)	26(1)	Z
106	43.844(1)	47(1)	Z
107	43.922(1)	23(1)	G
108	44.436(1)	16(1)	G
109	44.589(1)	19(6)	G
110	44.737(1)	12(1)	G
111	44.961(1)	15(1)	G
112	45.111(1)	20(2)	G
113	45.168(1)	40(2)	Z
114	45.405(1)	16(1)	G
115	45.850(1)	29(1)	Z
116	45.989(1)	22(1)	G
117	46.359(2)	63(7)	G
118	46.664(4)	311(5)	Z
119	46.803(1)	10(4)	G
120	47.282(1)	16(2)	G
121	47.478(8)	366(36)	G
122	47.851(1)	27	G
123	47.962(6)	238(23)	G
124	48.873(1)	17(1)	G
125	49.384(1)	90(3)	Z
126	49.676(2)	105(4)	Z
127	49.793(1)	15(3)	G
128	50.072(1)	90(4)	G
129	50.119(1)	56(10)	G
130	50.249(1)	24(4)	G
131	50.32(1)	483(30)	G
132	51.321(1)	65(3)	G
133	51.684(1)	48(3)	Z
134	52.04(1)	161(11)	Z
135	52.395(1)	27(4)	G
136	52.435(1)	76(2)	Z
137	52.795(1)	235(15)	G
138	53.114(2)	55(5)	Z
139	53.267(1)	19(1)	G
140	53.863(4)	88(10)	G
141	54.207(2)	101(5)	Z
142	54.488(1)	19(2)	G
143	54.932(1)	17(1)	G
144	55.263(1)	17(2)	G
145	55.431(1)	35(2)	Z
146	55.974(1)	131(13)	G
147	56.062(1)	144(33)	G
148	56.456(1)	149(4)	Z
149	56.668(1)	121(3)	Z
150	56.740(3)	4(4)	Z
151	56.768(1)	29(3)	G
152	57.556(1)	15(1)	G
153	57.753(1)	21(1)	G
154	57.978(1)	33(2)	G
155	58.135(1)	19(2)	G
156	58.239(1)	31(2)	G
157	58.987(1)	13(1)	G
158	59.179(1)	18(1)	G
159	59.718(2)	77(6)	G
160	59.890(1)	21(1)	G
161	60.111(2)	97(7)	G
162	60.637(1)	45(2)	G
163	61.104(1)	24(2)	G
164	61.522(1)	8(1)	G
165	61.667(1)	33(2)	Z
166	61.829(1)	53(5)	Z
167	62.348(3)	156(12)	G
168	62.600(2)	97(33)	G
169	62.804(1)	16(2)	Z
170	63.126(1)	16(1)	G
171	63.500(1)	5(1)	Z
172	63.524(1)	21(1)	G
173	64.078(1)	18(1)	G
174	64.535(1)	17(2)	G
175	65.089(1)	5(2)	G
176	65.334(1)	16(1)	G
177	66.287(1)	14(2)	G
178	66.375(1)	18(1)	G
179	66.898(1)	12(1)	G
180	67.186(1)	15(1)	G
181	67.333(1)	20(2)	Z
182	67.519(2)	72(6)	G
183	67.776(1)	6(3)	Z
184	68.243(1)	38(4)	G
185	68.426(1)	17(1)	G
186	68.642(1)	13(1)	G
187	68.875(1)	16(1)	G
188	69.200(1)	35(2)	G
189	69.728(2)	97(5)	G

Fano–Feshbach resonance positions, B, and widths, Δ, of the loss maxima shown in Fig. 1. For convenience, the loss features are reported in ascending order and labelled with index i. The error in brackets is 1σ. Δ is determined either from a Gaussian fit as the half-width at $1/e^2$ (method G) or by measuring the zero crossing of the resonance, B_{zero}, being $\Delta = |B - B_{zero}|$ (method Z).